Acta Materialia 105 (2016) 449–463

Contents lists available at ScienceDirect

Acta Materialia

journal homepage: www.elsevier.com/locate/actamat

Full length article

On the mechanisms of superplasticity in Ti–6Al–4V

E. Alabort [a], P. Kontis [b], D. Barba [a], K. Dragnevski [a], R.C. Reed [a, *]

[a] Department of Engineering Science, University of Oxford, Parks Road, Oxford, OX1 3PJ, United Kingdom
[b] Department of Materials, University of Oxford, Parks Road, Oxford, OX1 3PH, United Kingdom

ARTICLE INFO

Article history:
Received 28 September 2015
Received in revised form
1 December 2015
Accepted 2 December 2015
Available online 11 January 2016

Keywords:
Superplasticity
Titanium alloys
Grain boundary sliding
In-situ
Scanning electron microscopy

ABSTRACT

Surface observations are used to elucidate the deformation mechanisms responsible for the superplastic effect in Ti–6Al–4V. High-temperature *in-situ* tests for tensile and shear deformation modes are performed in the scanning electron microscope at temperatures in excess of 700° C. Grain boundary sliding is predominant; the micro-mechanics of accommodation are consistent with the dislocation-based Rachinger theory. The volume fraction of β plays a crucial role. For temperatures greater than 850 °C, the α grains remain unaffected; cavitation is minimal and slip bands needed for dislocation-based accommodation are detected in the β phase but are absent in α. At this temperature, grain neighbour switching is observed directly under shear deformation. At a temperature lower than 850° C, the β volume fraction is lower and a different mechanism is observed: slip bands in α and cavitation are found to accommodate grain boundary sliding. In addition, an increase in the α phase intragranular dislocation activity triggers the formation of subgrains and dynamic recrystallisation, consistent with the Rachinger dislocation creep effect. For temperatures lower than 700° C, superplasticity is absent; classical creep behaviour controlled by dislocation climb persists. A numerical treatment is presented which accounts for the Rachinger effect. The computational results are used to deconvolute the contributions of each of the competing mechanisms to the total strain accumulated.

1. Introduction

The mechanisms of superplasticity [1,2]– as observed in metallic systems based upon titanium, aluminium or iron – are controversial. Why? One reason may be that great emphasis has been placed – at least traditionally – on post-mortem analyses of microstructures at ambient temperature, or else deductions made *via* the analysis of the temperature- or stress-dependence of the strain rate. Clearly, this introduces a degree of uncertainty, since one cannot be completely sure of the underlying physical mechanisms which are operative on the critical scales: that of the grain size, the grain boundaries and the dislocations. Time-resolved *in-situ* observations would be invaluable in circumventing this difficulty and in elucidating the physical processes giving rise to the superplastic effect.

In particular, unequivocal proof concerning the precise details of the grain boundary sliding accommodation process – whether it is (i) diffusion-accommodated [3–5], (ii) dislocation-accommodated [6–8], (iii) a combination of both these [9,10] or (iv) some short of cooperative grain boundary sliding [11] – is still a matter of debate, in particular for the Ti–6Al–4V studied here. Experimentalists have developed methods to gather evidence for the underlying mechanisms, with mixed success. Surface studies are often used for this purpose. The first examinations used scratches to detect offsets of grain boundaries, using scanning electron microscopy. The latest studies use focused ion beam micromilled grids to study superplasticity in aluminium alloys [12]. However, all such studies rely on observations at ambient temperature. Alternatively, *in-situ* testing techniques [13–15] are expected to be significantly more powerful for the study of deformation mechanisms, particularly in cases where the volume fractions of the phases and their variation with temperature play a critical role.

Here, a new experimental method for the study of superplasticity is exploited. First, the mechanical behaviour of the titanium alloy is quantified using stress-relaxation tests at different temperatures. Second, surface studies are performed by *in-situ* testing – both in tension and shear – the material inside a scanning electron microscope. These observations of superplasticity are

* Corresponding author.
E-mail address: roger.reed@eng.ox.ac.uk (R.C. Reed).

http://dx.doi.org/10.1016/j.actamat.2015.12.003

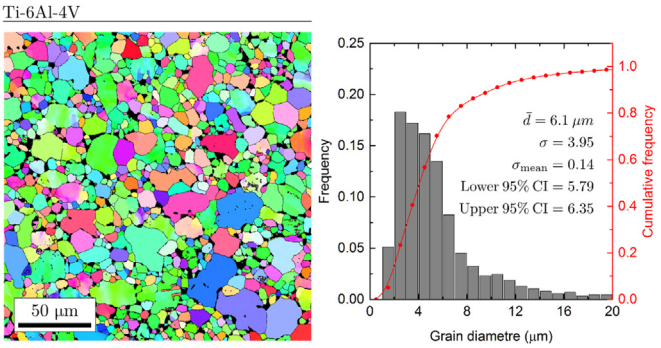

Fig. 1. Electron backscattered inverse pole figure map for α titanium and grain size distribution for the Ti–6Al–4V alloy.

carried out at different deformation regimes, pinpointed using an experimentally-derived strain-rate sensitivity map. Third, this new understanding of superplasticity is modelled analytically. This has allowed a deep appreciation of the factors causing superplasticity in Ti–6Al–4V to be gained.

2. Background

Superplasticity was discovered more than 80 years ago. Nowadays, it is widely – although not unanimously – believed that grain boundary sliding is the main deformation mechanism. But a question remains: how is this process accommodated? There are two main theories: *Rachinger* sliding [16] and *Lifshitz* sliding [17]. The former assumes that sliding is accommodated by dislocations in the lattice, whilst the latter that boundary mobility is a consequence of stress-driven diffusion. Unfortunately, these phenomenological descriptions do not include any details of the necessary accommodation mechanism which allows for continuity, *e.g.* at grain boundaries and triple points. Despite this uncertainty, most researchers [10,18,19] agree that a range of possible deformation mechanisms is likely, with the dominant one dependent upon temperature, strain rate and microstructural features.

Observations on deformed and initially plane-polished sections have been used to study superplastic deformation on the microstructural scale. Traditionally, such research has employed surface features such as fiducial markers to assess the micromechanics which are applicable [7,20–25]. However, it has not been until recently – when modern methodologies such as focussed ion beam micromilling and high-resolution electron backscattered diffraction (EBSD) have become widely available – that a number of studies have emerged providing direct and strong evidence of superplasticity in a number of different metals. For example, in the aluminium alloys AA5000, Rust and Todd [12,26] and Sotoudeh and Bate [27] have used sub-micron micro-milled markers to confirm that diffusion creep – and not dislocation activity – causes superplasticity. In contrast, Bate et al. [8,28,29] showed that dislocation slip rather than grain boundary sliding is the main deformation mechanism in the aluminium alloy AA8000. In iron-based alloys, surface analysis has been used to highlight the importance of dislocation activity, dynamic recrystallisation and grain boundary sliding in superplastic steels [30–32]. In magnesium alloys, texture analysis and marker observations have revealed that grain boundary sliding with no apparent intragranular dislocation creep controls the deformation [33]. Other studies suggest that dislocation slip and dynamic recrystallisation are active at large strains [34,35]. In zinc alloys, Xun and Mohamed [36,37] have used transmission electron microscopy to directly observe dislocations, proving that superplastic flow in Zn–22%Al is accommodated by slip. In titanium, surface scratches have been used to measure the amount of grain boundary sliding in Ti–6Al–4V with equiaxed [38] and lamellar microstructures [39]. Transmission electron microscopy has proven that dislocation activity is occurring within the α phase [40,41]. In addition, Lee et al. [42] have shown an effect of grain size on the amount of α phase dislocations present in superplastically deformed material. Since many distinct conclusions have been reported, it seems reasonable to believe that the mechanism of superplasticity may depend upon important alloy characteristics such as phase architecture and grain morphology. In general, one can conclude that more direct evidence is necessary before convincing answers can be given.

It follows that a difficult challenge arises when the material under scrutiny is a two-phase alloy, particularly when the volume fractions are highly sensitive to temperature. In these cases, post-mortem analyses may be insufficient; moreover, *in-situ* techniques offer significant advantages. Although the use of *in-situ* observations is not new – research applying these techniques has been reported for the study of superplastic deformation [43,44,9,21,45,25] – studies have yet to be reported on the use of *in-situ* scanning electron microscope testing for the study of high-temperature superplasticity. In Ti–6Al–4V, for which the volume fraction of β phase at optimal superplastic temperature is four times the volume fraction at room temperature, *in-situ* tools are indispensable. Due to differences in the basic crystallography – HCP for α and BCC for β phase respectively – the deformation behaviour of each phase is substantially dissimilar. Thus, it has been shown that at elevated temperatures β is considerably softer than α [46,47]. This effect is generally attributed to a higher diffusivity and more active slip systems in β than its α counterpart. Therefore, in either diffusion- or dislocation-controlled superplasticity, it would be reasonable to assume that it is the volume fraction of β which plays the critical role in determining the dominant mechanism.

Why is this important? One of the main challenges of superplastic forming is to improve the efficiency of manufacturing, but also to expand its range of applicability [48]. This generally means lowering the forming temperature [49] and reducing the forming time [50]. In titanium alloys, this is accomplished in two different ways: (i) by optimising the microstructure to enhance superplasticity – *i.e.* by refining the grain size [51] and/or by increasing the β fraction [52] or (ii) by pushing the processing conditions outside the optimal window of superplastic formability – thus processing at lower m values. One way or the other, practitioners would benefit from a better understanding of the underlying physics and the microstructural consequences of deformation in different regimes.

With the above in mind, the purpose of the present paper is to carry out detailed observations with the aim of confirming unequivocably the mechanisms of superplastic deformation in Ti–6Al–4V at different forming regimes. In the first part of this work, the superplastic effect in Ti–6Al–4V is quantified using stress-relaxation tests. The results are used to propose a matrix of experimentation across which different micro-mechanisms are expected – *i.e.* different strain rates and temperatures. Second, surface observations are performed at temperature using a newly-developed *in-situ* scanning electron microscope testing module. To study the relative motion and deformation of grains, microgrids are milled into the sample surface. Finally, a numerical representation

Table 1
Chemical composition for the Ti–6Al–4V alloy (wt. %) used in this study.

Al	V	Fe	O	C	N	H
5.5–6.5	3.5–4.5	0.25	0.13	0.08	0.05	0.0125

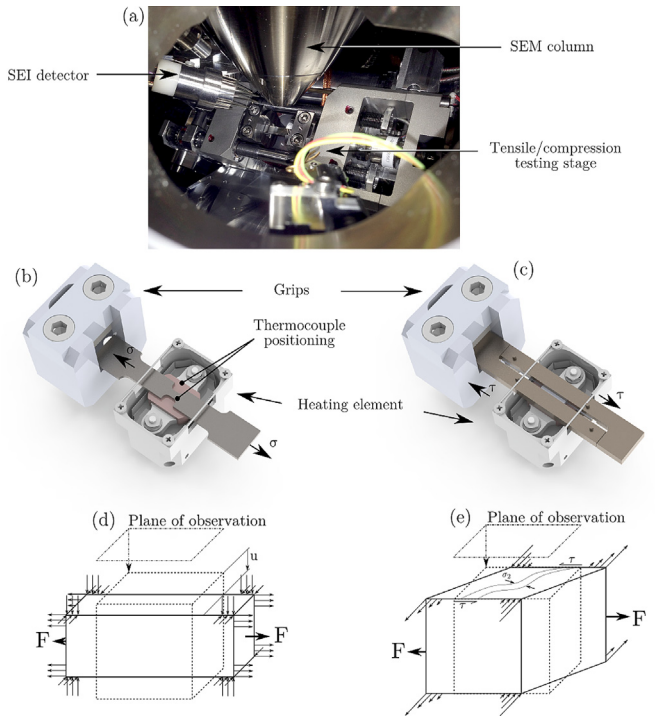

Fig. 2. (a) Tensile testing stage positioned inside the SEM chamber. (b) Design of the tensile testing experiment showing the arrangement of the grip-heater-sample. (c) Arrangement of the shear testing rig. Image shows the geometry of the arrangement which translates the uniaxial movement of the grips into a state of simple shear in the specimen. (d) Deformation state during tensile testing and (e) tension and compression stresses during shear testing.

of the mechanics of deformation is proposed. The results are used to elucidate the deformation mechanisms causing superplastic and close-to-superplastic deformation in this alloy.

3. Method

The titanium alloy Ti–6Al–4V studied exhibits a microstructure typical of the material used for superplastic processing: equiaxed α phase grains with small amounts of intergranular β phase. The mean grain size was approximately 6.1 μm, as verified using electron backscattered diffraction (EBSD) analysis. Fig. 1 shows an inverse pole figure map of a representative area and the grain size distribution. The mean grain size was estimated according to [53] as

$$\overline{d} = \frac{\sum A}{\sum d_{\mathrm{ceq}}} \tag{1}$$

where A is the grain area and d_{ceq} is the grain diameter. Its chemical composition is given in Table 1.

3.1. In-situ observations

A series of superplasticity tests were performed using a high-temperature micro-tensile testing stage, placed inside the chamber of a high-resolution scanning electron microscope (SEM). The module was fitted with a resistance heater capable of reaching temperatures up to 1000° C. The temperature of each specimen was monitored using thermocouples fitted between the sample and the heater; a further thermocouple wire spot-welded on the sample surface was used in each case for verification purposes. Tungsten wire springs were used on each side of the furnace to ensure an appropriate contact between the specimen and the heater surface. To improve the thermal conductivity, gold leaves were strategically positioned between heater and specimen. The experimental arrangement is illustrated in Fig. 2.

Tensile tests were performed at 700, 800 and 900° C at strain rates of 3×10^{-3}/s and 2×10^{-4}/s. Samples were paused every 10% increment in tensile strain to perform SEM imaging. Shear tests were performed at temperatures of 750 and 850° C and a shear strain rate of 2×10^{-4}/s. Shear conditions were limited in both temperature and strain rates due to risk of buckling. Image periodicity was decreased to every 25% increment in shear strain to reduce any influence on the superplastic deformation. Imaging setting was optimised in order to keep each interruption below 90 s: 30 s holding period – where load-relaxation occurred – and 60 s for imaging. After image acquisition, the test was resumed using identical displacement-controlled conditions: the same level of stress prior interruption was observed.

For tensile deformation, double dog-boned samples were extracted from Ti–6Al–4V sheet; samples were designed with a small gauge portion of dimensions 5 mm length × 2 mm width × 0.75 mm thick. For shear tests, samples were designed with a gauge volume of 10 mm length × 1.5 mm width × 0.75 mm thickness. This ensured that the main deformation could be captured by scanning electron microscopy without compromising significantly the minimum representative volume of the material. The sample surface was then prepared for metallographic examination in the usual way. In order to facilitate the assessment of the sample surface during shear deformation tests, microgrids were milled using a focused ion beam instrument. A regular grid of dimensions 100 × 100 μm with a pitch of 5 μm and 1 μm deep was chosen.

3.2. Load relaxation tests

Load-relaxation tests are performed using an electro-thermal mechanical testing (ETMT) machine at temperature range between 700 and 950 °C with 50 °C intervals. This technique is able to quantify the strain rate sensitivity parameter, m, and has advantages over conventional methods such as strain-rate jump tests [42,54–56]. Here, testing involved the loading of the material at constant strain-rate until a predefined strain (4%) was reached – this was enough to achieve steady-state stress behaviour. Then, the cross-head displacement was stopped – and maintained in that exact position – while the load relaxation was recorded as a function of time. Since the displacement is blocked, the strain-rate of the system must be in equilibrium according to

$$\dot{\varepsilon}_{\mathrm{p}} + \dot{\varepsilon}_{\mathrm{e}} + \dot{\varepsilon}_{\mathrm{m}} = 0 \tag{2}$$

where $\dot{\varepsilon}_{\mathrm{p}}$ is the sample plastic strain-rate, $\dot{\varepsilon}_{\mathrm{e}}$ is the sample elastic strain-rate and $\dot{\varepsilon}_{\mathrm{m}}$ is the elastic strain-rate of different parts of the testing apparatus. The plastic strain-rate can be expressed as

$$\dot{\varepsilon}_{\mathrm{p}} = -\frac{\dot{\sigma}}{E} - \frac{A\dot{\sigma}}{Lk_{\mathrm{m}}} \tag{3}$$

where A is the sample cross-sectional area, E is the sample elastic modulus, k_{m} is the stiffness of the machine, $\dot{\sigma}$ is the change of stress with time ($\mathrm{d}\sigma/\mathrm{d}t$) and $A\dot{\sigma}$ is an approximation of the change in the applied force ($\mathrm{d}P/\mathrm{d}t$). One can see that the plastic strain-rate is proportional to the slope of the stress-relaxation curve consistent with

$$\dot{\varepsilon}_{p} = -M\dot{\sigma} \tag{4}$$

where M is the apparent elastic modulus of the material previously

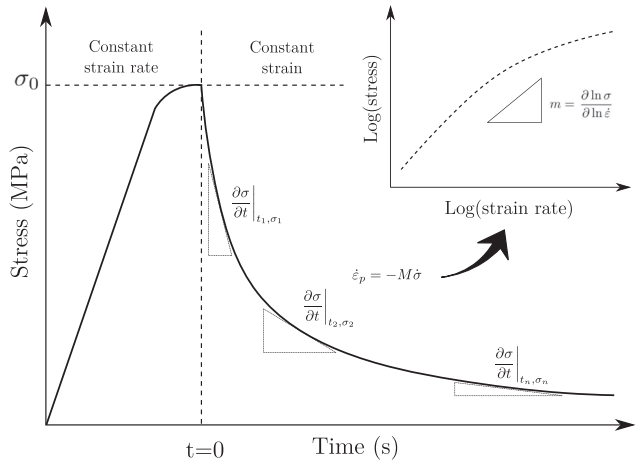

Fig. 3. Representation of the methodology followed to derive the stress-strain rate response and the strain-rate sensitivity parameter m from the series of load-relaxation tests.

expressed as

$$M = \frac{1}{E} + \frac{A}{Lk_m}. \quad (5)$$

Unfortunately, the stiffness of the machine k_m is not known. For its estimation, one can introduce the following assumption: when the specimen is still under elastic deformation, the apparent elastic modulus of the material is described by

$$M = \frac{X}{L\sigma} \quad (6)$$

where X (X=X_e+X_M) is the displacement of the cross-head; in practice this includes a contribution from both the elastic displacement of the specimen (X_e) and the elastic displacement of different parts of the machine (X_M). The apparent elastic modulus M decreases with increasing plastic strain, hence some error can be introduced in the derivation of the strain-rate sensitivity m due to the estimation of M, but since $E \ll k_m$, this effect is likely to be small.

For stress-relaxation testing, specimens of geometry 40×2×1 mm were machined using electro-discharge machining (EDM). To remove the effects of any damaged layer induced by EDM machining, care was taken to grind the appropriate surfaces using 600 grit SiC abrasive paper.

4. Results

4.1. Stress relaxation in superplasticity

In the first instance, the regime of superplasticity was determined by deducing the strain-rate sensitivity parameter m using stress-relaxation tests by following the procedure shown in Fig. 3. The processed stress-strain rate data for temperatures between 700 and 950° C at strain rates between 1×10^{-2} and 1×10^{-6}/s are shown in Fig. 4 (a), covering the anticipated range of conditions at which superplasticity might be operative.

The stress-strain rate curves were then analysed to measure the strain rate sensitivity parameter m which is defined as a function of the logarithmic values of stress and strain rate as

$$m = \frac{\partial \ln \sigma}{\partial \ln \dot{\varepsilon}}\Big|_{\varepsilon,T} \quad (7)$$

where σ and $\dot{\varepsilon}$ are the stress and the strain rate for a given value of strain ε and temperature T. The derived strain rate sensitivity map is presented in Fig. 4(b) for a value of strain of 0.04. An optimal strain rate sensitivity is found at temperatures higher than 800° C and strain rates slower than 1×10^{-3}/s. For these conditions, m is consistent with values characteristic of Region II superplasticity. A maximum value, m=0.51, is found at 900° C and 1×10^{-4}/s. It is widely accepted that above the optimum strain rate – around 1×10^{-3}/s for the material studied – the parameter m decreases due to dislocation creep being the dominant mechanism.

With the above, one can define an experimental testing programme which targets different behavioural regimes. Here, a series of *in-situ* tensile and shear tests were carried out at different deformation conditions with aim of providing time-resolved

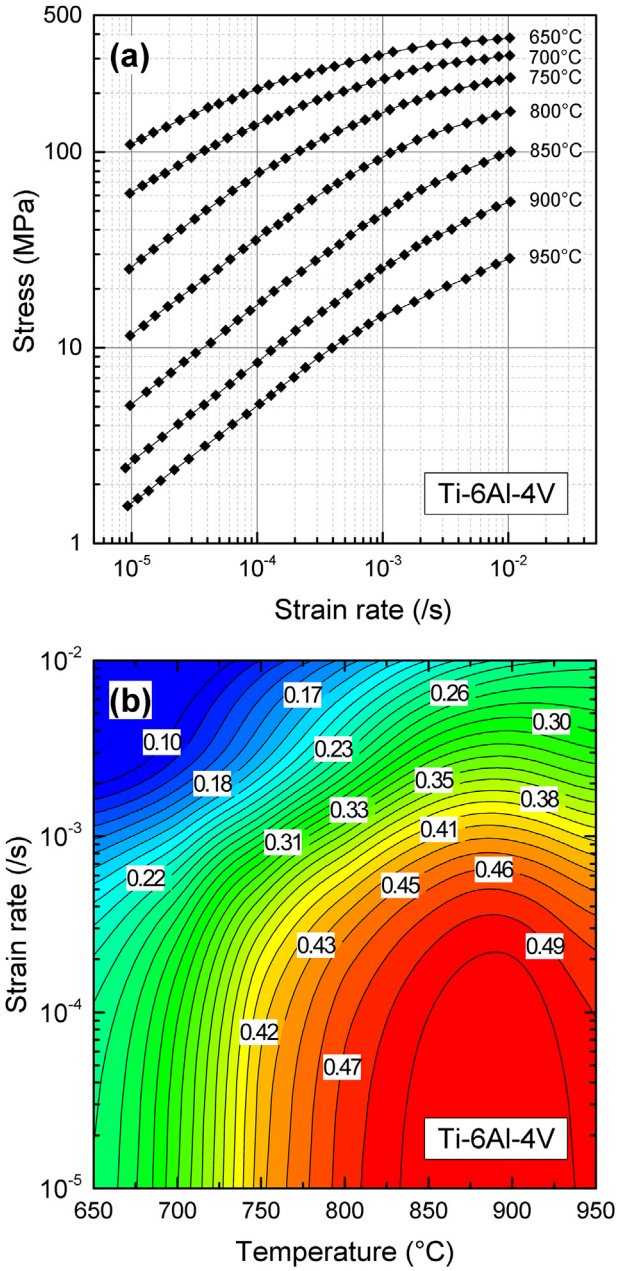

Fig. 4. (a) Stress dependence of strain rate of Ti–6Al–4V at temperatures between 650 °C and 950 °C obtained by stress relaxation techniques. (b) Contour map of the strain rate sensitivity exponent m as a function of temperature and strain rate. Derived using the slope from the curves presented in Fig. 4(a).

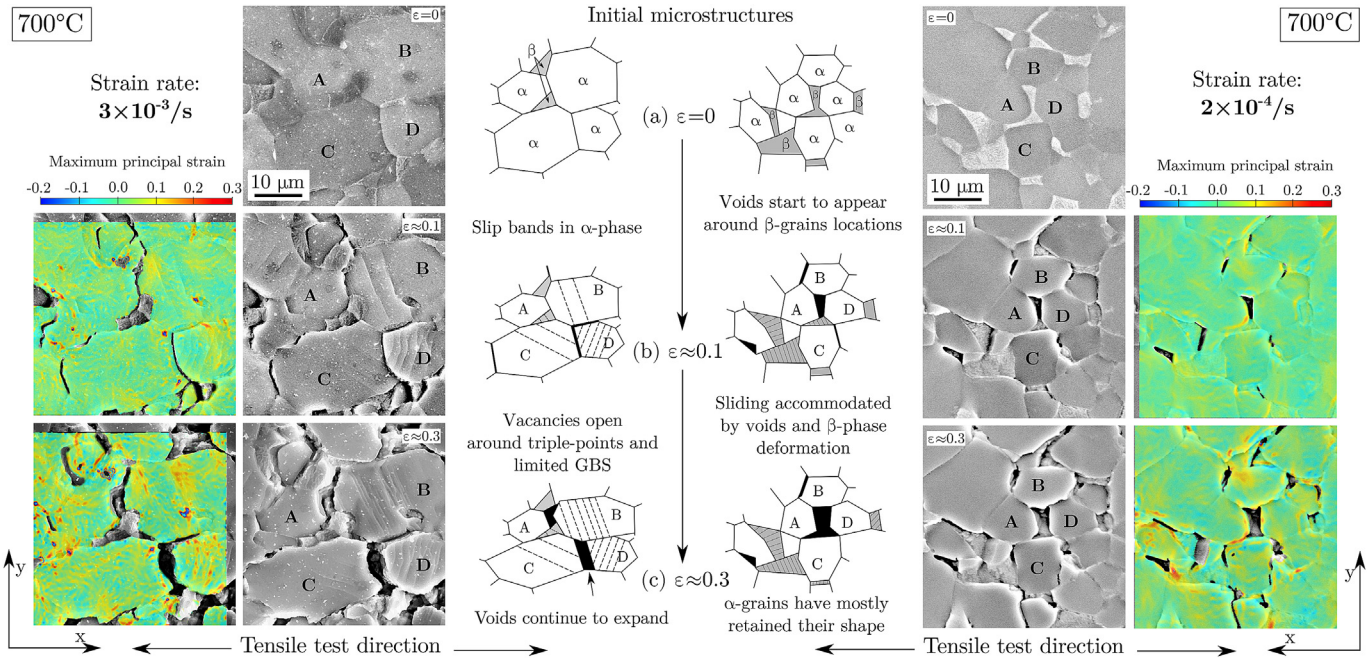

Fig. 5. Micrographs of a Ti–6Al–4V sample tested at 700 °C applying strain rates of 3×10^{-3}/s and 2×10^{-4}/s and paused for levels of strain of: (a) initial state; (b) 10% strain; (c) 30% strain. An estimate of maximum normal strain, determined using digital image correlation, is provided next to each relevant SEM micrograph.

observations of the different mechanisms which are operating.

4.2. Tensile mode surface observations

Results at 700° C and strain rates of 3×10^{-3} and 2×10^{-4}/s are given in Fig. 5. Grain boundary sliding is observed under both rates of deformation. At this temperature, there is little β phase present and this seems to facilitate the sliding of α grains by pinching off at critical grain boundaries as appreciated in Fig. 5(b). For a strain-rate of 3×10^{-3}/s, the motion of grains is accommodated by the opening of cavities and intragranular deformation; slip bands are evident and elongation along the tensile direction is found. For the lower strain rate (2×10^{-4}/s), the material response is distinct; slip bands are absent.

Digital image correlation (DIC) was used to measure intragranular strains. DIC is able to quantify the accumulation of strain surrounding the slip bands, showing that the majority of the strain contribution at 700° C and 3×10^{-3}/s comes from intragranular deformation of α grains. At lower strain rates, the decrease in α-lattice deformation is compensated by an increase in grain boundary sliding. This change in mechanism is also found in the derived strain rate sensitivity map presented in Fig. 4(b). The parameter m is shown to increase from Ref. m=0.18 (climb controlled creep in region III) when deforming at a strain rate of 3×10^{-3}/s, to m=0.3 (a relatively low value for superplasticity in region II) when a strain rate of 2×10^{-4}/s is imposed.

The material response at 900° C and 2×10^{-4}/s is different, see Fig. 6. Whilst in some ways similar to that at 700° C, it is representative of a true superplastic effect (m>0.4). At this temperature, the volume fraction of β phase is higher, 45% of the total volume [57]. In terms of phase growth kinetics, the small amount β present at ambient temperature seem to grow in an analogous way to that described by Seward et al. [58]; there is a competitive growth between intragranular plates and grain boundary β that expands towards the interior of α grains. The microstructure at 900° C is clearly revealed once deformation begins, see Fig. 6(b) and (c). At this point, the β phase is no longer a grain boundary phase exclusively and although it seems to behave similarly to α phase, certain differences are found.

Contrary to the observations reported at 700° C, α grains retain their initial shape even after high levels of strain. Relative grain translation and grain realignment along the tensile direction is clear. This translation is mainly accommodated by the deformation of β grains. Although slip deformation within β phase is observed, significant elongation is not and grain boundary sliding can be accommodated by dislocation activity while the microstructure stays equiaxed. In Fig. 6(c) and (d) grains have appeared beneath the surface around the set of α grains that were initially together in Fig. 6(a), three-dimensional rotation and translation of grains play an important role at this temperature. Surface observations show that grain boundary sliding is accommodated by the creation and annihilation of β-filled cavities, grain boundary mobility and intragranular slip deformation of β grains.

At 650° C and 10^{-3}/s, the superplastic effect is absent. SEM micrographs at two different time/strain points are presented in Fig. 7(a) and (b), showing the microstructure at 0 and 30% strain respectively. For strains higher than 30%, grain elongation is clear. Intragranular plastic deformation (in the form of slip bands) is observed directly and no relative grain sliding is evident. Fig. 7 shows that A-B-C-D grain boundaries remain unchanged. The bulk of deformation can be attributed to dislocation activity in the α phase. Since each grain has different crystallographic orientation and hence a limited number of slip systems, grains tend to reorientate along the testing direction. Rotation is conferred by the motion of dislocations confined in the interior of the grains. The dislocation density and therefore, the number of visible slip bands, tend to increase with deformation as appreciated in the micrograph series. This behaviour is typical of classical warm plasticity.

4.3. Shear mode surface observations

Surface observations obtained in shear are in agreement with

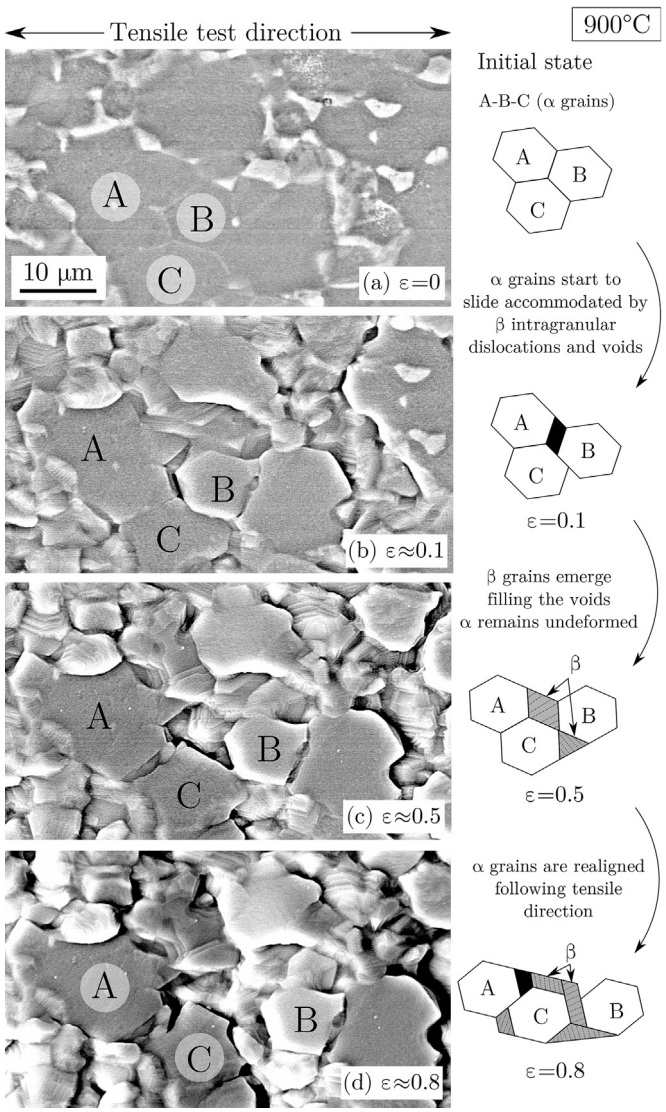

Fig. 6. Micrographs of a Ti–6Al–4V sample tested at 900 °C applying a strain rate of 2×10^{-4}/s. The SEM micrographs were taken at levels of strain of: (a) initial state; (b) 10% strain; (c) 50% strain and (d) 80% strain.

those in tension. But, a more constrained surface in the plane of view allows the observation of phenomena unattainable otherwise – for example, the switching of grain boundary neighbours. However, shear deformation involves a more complex state of stresses. In order to facilitate the optical assessment of the surface at high strains, grids were micromilled onto the specimen surface.

Fig. 8 shows the surface of a sheared sample before and after being deformed. The macroscopic strain derived from the machine crosshead displacement (γ=0.5) is in close agreement with the microscopic strain measured from the grid shearing (γ=0.4). The internal FIB milled grids show unequivocal signs that grain boundary sliding occurs. The offset of grid lines in the boundaries of grains proves that relative grain translation and rotation are part of the mechanism of deformation. Small amounts of intragranular deformation are also present – grains elongate following the stress state introduced during shearing, see grains C and F in Fig. 8. Grains with an area larger than the mean grain size tend to deform the most; smaller grains minimise intragranular creep and enhance grain boundary sliding. Out-of-plane grain sliding is also observed. For instance, grains A and D have reduced their exposed area. For grain A, 3 complete grids (●) were visible in Fig. 8(a), after 0.5 shear strain, only one and a half grids (○) are recognizable, the rest of grain A has slid under grain B. Similar conclusions can be drawn from the reduction of vertical grids among the pair of grains D and E.

At this temperature, there is not enough β phase to accommodate the sliding of grains; as a result, dynamic recrystallisation (DRX) occurs. Its mechanics of accommodation are illustrated in the series of micrographs shown in Fig. 9. During DRX, subgrains develop due to the conversion of dislocation cell walls into secondary grain boundaries [35]. For grain A, subgrain boundaries begin to form when a 10% shear strain is reached – Fig. 9(b). Then, subgrains such as those labelled a_1-a_2-a_3-a_4-a_5 begin to recrystallise and separate. Fig. 9(c) and (d) show these new grains sliding and rotating in different directions as the deformation continues.

At 750° C, the switching process of grain neighbours is observed directly in Fig. 10. The switching is found in the first place among the group of grain A-B-C-D and it is assisted by out-of-plane sliding: grain A slides over grain B, closing the distance to grain C. When a shear strain of 0.75 is reached, grains A and C are in contact – the neighbour switching process is completed. For a shear strain larger than 1, half of grain B has slid under grain A, the switching process continues. When a shear strain of 1.5 is attained, grain A is in contact with grain a and this is assisted by the appearance of cavities between grains A-C-D. Identical mechanics are found between grains C-c-b-e, but in this case, grain b slides over grain C until it reaches a sharing position with grain e.

Results obtained in shear at 850° C are similar. Fig. 11 illustrates the gridded surface before and after a shear strain of γ=1.5 is reached. A series of micrographs show details of the grain rearrangement between grains A-B-C-D. At low strains, the sliding of these grains is accommodated by slip deformation of β; see Fig. 11(b) and (d). At higher strain, β cannot fully accommodate the process and α grains begin to distort – particularly around the grain boundaries – in order to complete the switching of grain neighbours. This effect is illustrated with grains B and D in Fig. 11(e) and (f). At this temperature and deformation rate, dynamic recrystallisation is not found.

5. Rationalisation of the observations

Historically, the use of surface observations for the study of superplasticity has been criticised: is the material surface truly representative of the bulk behaviour? What are the limitations? First, it is important to note that observations are performed on a free-surface – *i.e.* there are different boundary conditions than in the bulk. For deformation in tension, this means that grains can shear freely in the out-of-plane direction. When grains move towards the outer plane, the so-called 'floating grain' effect can occur [9]. Grains no longer deform in harmony with the bulk; they retain their initial shapes and drift as the movement of inner material layers dictates. This means that any artefacts due to deformation in tension might be presented as an absence of deformation; any conclusion extracted from grains being deformed must, therefore, be valid. Nonetheless, careful consideration should be given to the amount of cavitation and grain translation reported under tension, for in shear, out-of-plane displacement is minimised [59]. The combination of both deformation modes should give a global and valid view of the deformation mechanisms of superplasticity.

Second, even though tests are performed under vacuum, oxidation occurs. Previous studies have highlighted the kind of misinterpretation that thin layers of oxide can induce [12]: (i) oxide can leave ghosts of prior grain positions and (ii) striated surfaces or ligament formation can appear close to triple point boundaries. In

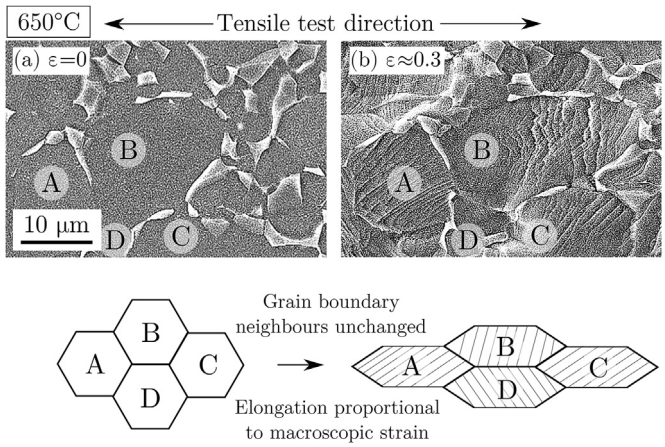

Fig. 7. Micrographs of Ti–6Al–4V sample tested at 650 °C at a strain rate of 10^{-3}/s and levels of strain of: (a) initial state and (b) >30% strain.

our study, reduced amounts of oxide pile-up at the grain boundaries can be found in shear – but none in tension. It seems unlikely that such an effect would be large enough to invalidate the conclusions here reported. However, the oxide layer affects the quality of the microgrid, limiting the optimal pitch size to approximately 4 μm. With the above in mind, one can carefully begin to rationalise the results with possible artefacts and other effects taken in consideration.

5.1. On the deformation mechanisms of superplasticity

The main findings of the results given above are to our best knowledge the first high-temperature *in-situ* observations of this phenomenon in Ti–6Al–4V. The surface observations prove that dislocation activity – either α or β – is the phenomenon accountable for the accommodation process of grain boundary sliding responsible for superplasticity in Ti–6Al–4V – and possibly other superplastic systems.

For low-temperature superplasticity (700–800° C), α grains behave as a skeleton, carrying out the main deformation with β playing a secondary role in the grain boundaries. Intragranular creep of α phase is shown to accommodate the grain boundary sliding aided by the appearance of cavities and voids [60]. As the deformation continues, accumulation of dislocations activate the formation of subgrain boundaries which leads to dynamic recrystallisation. At intermediate temperatures (800–850° C), a slight increase in the volume fraction of β facilitates the rearrangement and sliding of α grains. At these temperatures, the intragranular deformation of α is reduced, no slip deformation bands are found, but a certain amount of cavitation and distortion around a peripheral *mantle* are still present. For high-temperature superplasticity (> 850° C), the α phase becomes less important as the proportion of the soft deformable β increases. In this regime, the rate-controlling process is the intragranular slip of β. Cavitation is minimised and recrystallisation does not occur.

As per the traditional definition of superplasticity, the switching of grain boundaries needs to occur. But the micromechanisms of switching here elucidated are different to those found in superplastic aluminium [12,27] – intragranular slip is observed directly and diffusion of matter seems unlikely. The process has been observed both in shear and in tension, but distinct mechanics are operative. For in shear, grain boundaries forming a 45° angle with the shear direction and parallel to the local state of compression are found more likely to switch neighbours; see Fig. 12(a). Two examples are discussed: (i) at 750° C (Fig. 10), the switching of grains A-B-C-D seems to follow the kind of process illustrated in Fig. 12(a): grains move towards the directions imposed by the local state of stress. The accommodation is assisted by out-of-plane sliding, with grains that fold three-dimensionally in an *origami* fashion. (ii) At 850° C (Fig. 11), no out-of-plane sliding is perceived, but the grain lattice deforms to allow continuity during the switching process. It seems that the local boundary orientation angle θ is critical. If θ is close to 90°, out-of-plane sliding is restricted – intragranular slip is more likely. For in tension, grain neighbour switching also occurs. In this case, the switching is found in the shearing planes created by the tensile stress. These shearing planes are located perpendicular to the plane of observation so that the process cannot be observed directly. However, the emergence of inner-plane grains – which is a consequence of this internal switching – is reported in Fig. 6.

5.2. Rachinger grain boundary sliding

Many theoretical explanations of the micromechanics of superplasticity are available in the literature. Unsurprisingly, a common resemblance is found: the Rachinger grain boundary sliding (GBS) effect [61]. Rachinger GBS is characterised by a particular set of features. First, the net number of grains along the tensile axis must increase with deformation. In Fig. 6, α grains realign along the tensile axis, accommodated by the appearance of sub-surface β grains. Second, intragranular strains must be small in order to keep grain equiaxiality. Fig. 5 shows that, at optimal strain rates, intragranular strain is severely reduced. In shear, α slip deformation bands are not observed, but minor grain elongation is necessary. Third, for this to happen at high strains, grain neighbour switching is needed. This process has been discussed in Figs. 10–12, showing direct and precise details of the mechanism. Fourth, a disappearance of texture must be found. This has been proven previously [62] in the same Ti–6Al–4V alloy for the exact range of deformation conditions studied here.

Rachinger sliding requires lattice dislocations to move in order to accommodate the sliding of grains. It is well-established that the details of this process are controlled by the equilibrium subgrain size parameter λ which can be expressed as [63]:

$$\frac{\lambda}{b} = \zeta\left(\frac{\sigma}{\mu}\right)^{-1} \tag{8}$$

where b is the magnitude of the Burgers' vector, σ is the stress, μ is the shear modulus and ζ is a constant. Here, the mean grain size is constant, but the parameter λ is dependent upon the applied stress and hence, a function of the processing conditions. Fig. 4(a) is used to construct an equilibrium subgrain size contour map for Ti–6Al–4V; results are presented in Fig. 13 for a value of ζ=35. The superimposition of Figs. 13 and 4(b) highlights a clear effect: a subgrain size parameter λ greater than the mean grain size d is needed so that a superplastic strain rate sensitivity parameter can be achieved (m>0.36). Theory says: (i) for a grain size greater than the subgrain size, intragranular dislocations will form subgrains [64]. This means that lattice slip dislocations pile up in the grain lattice forming intragranular subgrain boundaries; (ii) for a grain size below the subgrain size λ, superplasticity will be active [61]. In this case, no subgrains form; the intragranular dislocations travel along the lattice until the opposing grain boundary is found.

Direct observations which prove each one of these cases were found. Fig. 14(a) shows how the accumulation of stress in the triple point grain boundary of a given α blocking grain triggers the

formation of subgrains which leads to dynamic recrystallisation. As straining continues, the subgrains recrystallise forming new α grains. This behaviour is typical of the close-to-superplastic high-strain-rate regime. However, when the equilibrium subgrain size exceeds a critical value, $d<\lambda$, no subgrain formation is observed and the optimal superplastic regime is found. In this case, the stress induced by grain boundary sliding into blocking grains is translated into dislocations fully travelling through the softer β grain lattice, leading to intragranular slip as shown in Fig. 14(b). The β volume fraction is believed responsible for the transition from high-temperature dislocation creep to superplastic grain boundary sliding. Furthermore, both regimes have been observed active under the same conditions due to a wide distribution of the local grain size as illustrated in Fig. 15. With this in mind, one can find two ways to improve the superplastic efficiency in titanium alloys: (i) the mean grain size can be reduced, enlarging the area in which the constraint $d<\lambda$ is satisfied or (ii) the volume fraction of β can be increased by β-stabilising the alloy. Both options are known

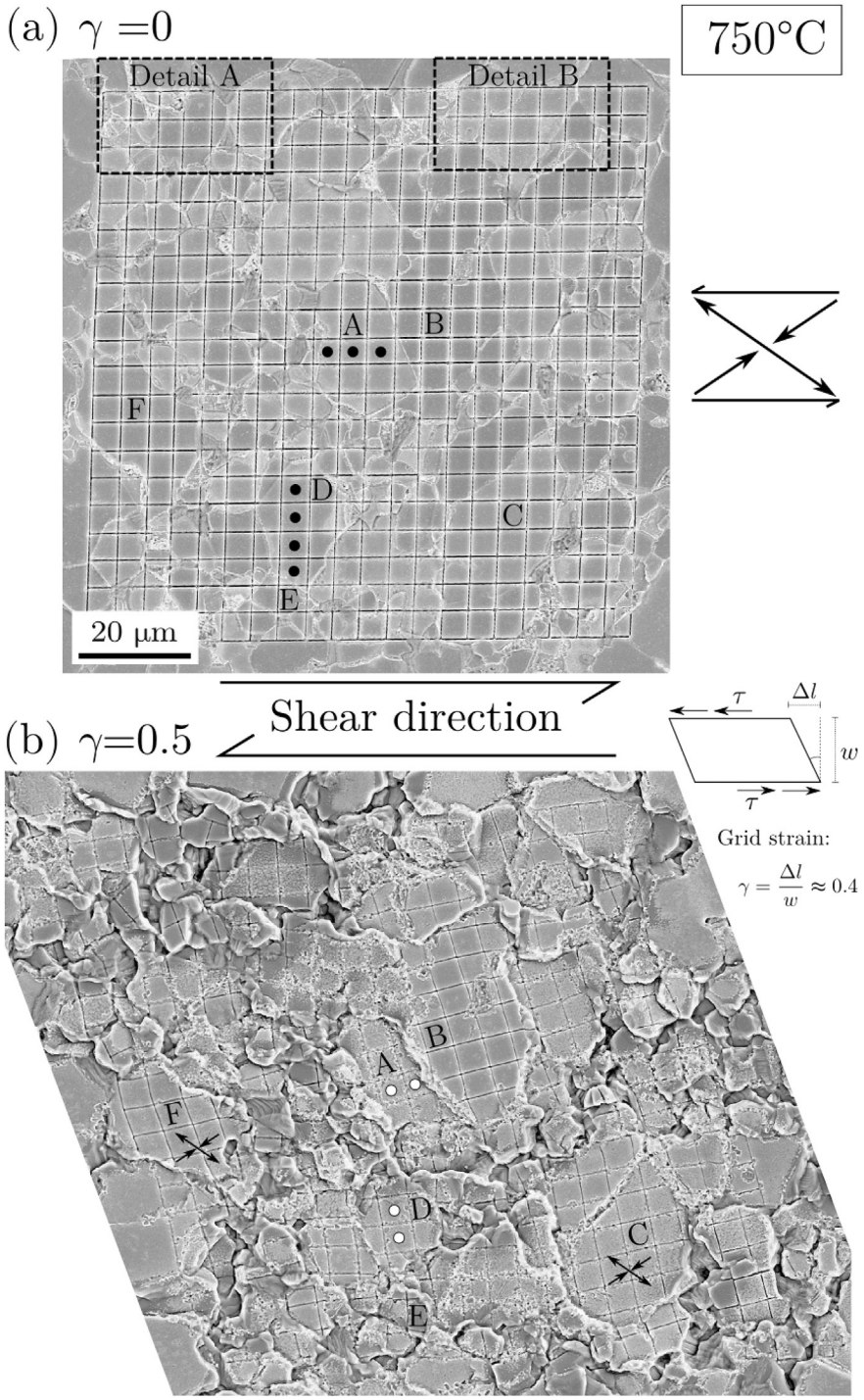

Fig. 8. Microgridded surface of Ti–6Al–4V tested in shear at 750 °C at a shear strain-rate of 2×10^{-4}/s at: (a) initial configuration and (b) shear strain of 0.5. Areas marked as (●) and (○) are used to identify the number of visible grids on grains A and D after and before deformation respectively.

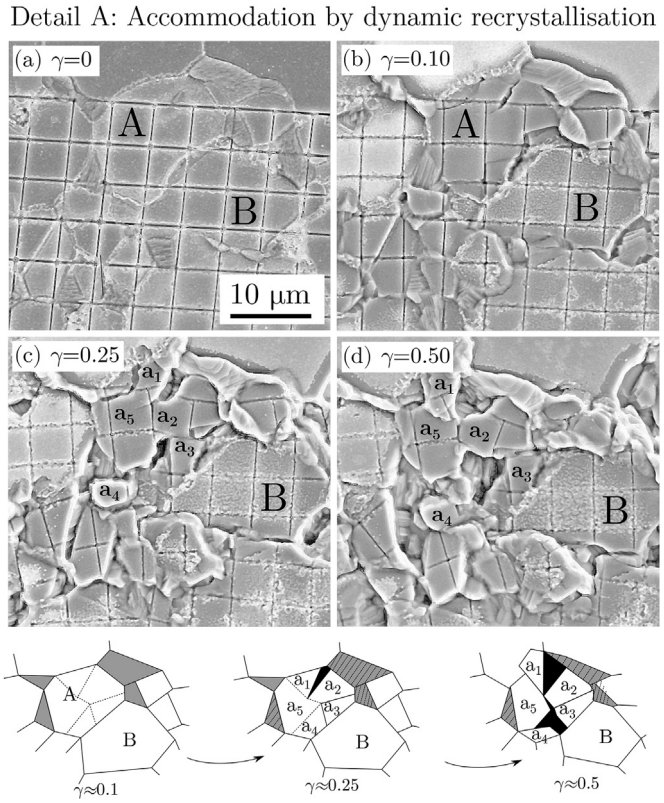

Fig. 9. Detail of the subgrain formation process during a shear test at 750 °C in the area marked A in Fig. 8. Micrographs are shown at shear strains of: (a) γ=0, (b) $\gamma \approx 0.1$, (c) $\gamma \approx 0.25$ and (d) $\gamma \approx 0.5$.

to improve superplasticity in titanium alloys, but here, a method that physically explains and measures the transition has been provided – see Fig. 13.

6. Numerical treatment of superplasticity in Ti–6Al–4V

6.1. A representation of Rachinger grain boundary sliding

High-temperature deformation – or creep – is generally a thermally-activated process for which the rate of deformation is controlled by the speed of a diffusional mechanism. Thus, the steady-state strain rate, $\dot{\varepsilon}$, is commonly expressed as [63].

$$\dot{\varepsilon} = \frac{AD\mu b}{kT}\left(\frac{b}{d}\right)^{p}\left(\frac{\sigma}{\mu}\right)^{n} \tag{9}$$

where D is the diffusion coefficient, μ is the shear modulus, b is the magnitude of the Burgers' vector, k is the Boltzmann constant, T is the temperature, σ is the stress, d is the grain size, A is a material constant and p and n are the grain size and stress exponents respectively.

Considering the regimes studied here, it has been found that superplastic deformation in Ti–6Al–4V needs to be rationalised by considering dislocation creep accommodated grain boundary sliding by both α and β phases but also superplastic grain boundary sliding [65]. Equations for each one of these processes are now proposed and assumed to compete for the role of dominant mechanism [66]. Then, material parameter optimisation techniques can be used to empirically determine the values of each set of equations with the aim of establishing and quantifying the contribution of each micromechanism.

Regarding the deformation mode, controversy exists concerning whether the iso-stress [67,38], the iso-strain mode or a combination of both [46] is the most appropriate representation of the multi-phase behaviour in Ti–6Al–4V. Even though both deformation modes have been shown to deliver good results at the macroscopic level, one must note that both assumption are inadequate at the microstructure level – in mesoscopically heterogeneous microstructures neither the stress nor the strain can be homogeneous. Limitations considered and caution advised, a homogenisation approach is used for simplification: the total macroscopic strain-rate is decomposed following the iso-stress assumption as

$$\dot{\varepsilon}_{t} = \dot{\varepsilon}_{\alpha}(1 - f_{\beta}) + \dot{\varepsilon}_{\beta} f_{\beta} + \dot{\varepsilon}_{gbs} \tag{10}$$

where $\dot{\varepsilon}_{gbs}$ is the rate of strain due to grain boundary sliding, $\dot{\varepsilon}_{\alpha}$ and $\dot{\varepsilon}_{\beta}$ are the rate of intragranular creep deformation for α and β phases respectively and f_{β} is the volume fraction of β phase as a function of temperature.

The strain rate contributed by each phase can be expressed as

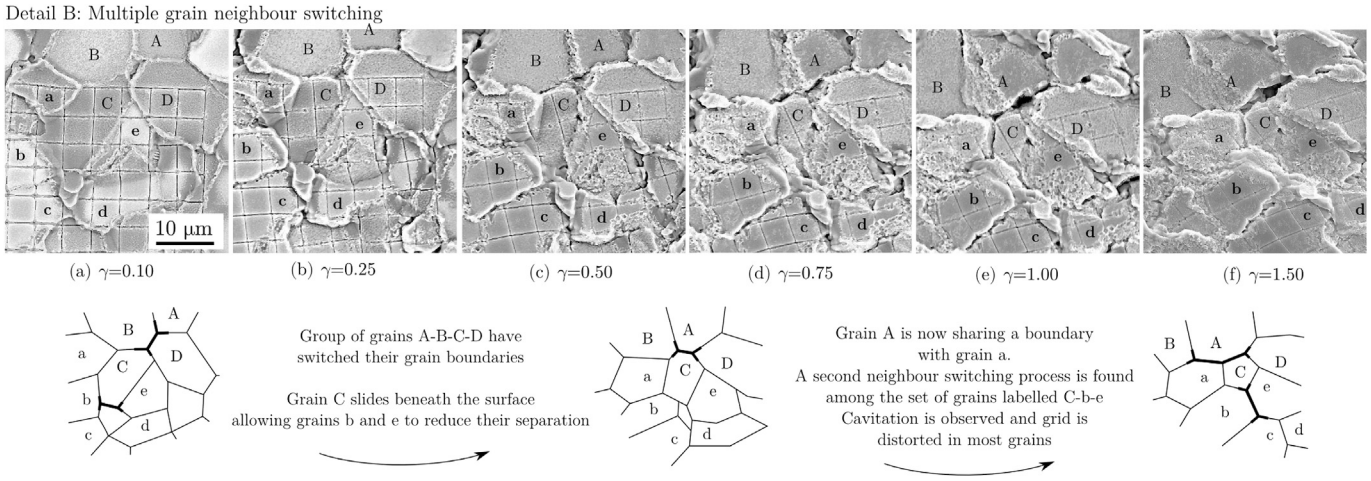

Fig. 10. Detail of the grain neighbour switching process during a shear test at 750 °C in the area marked B in Fig. 8. SEM micrographs are shown at shear strains of: (a) γ=0, (b) $\gamma \approx 0.25$, (c) $\gamma \approx 0.5$, (d) $\gamma \approx 0.75$, (e) $\gamma \approx 1.0$ and (f) $\gamma \approx 1.5$.

$$\dot{\varepsilon}_{\alpha,\beta} = \frac{A_{\alpha,\beta} D_{\alpha,\beta} \mu_{\alpha,\beta} b}{kT} \left(\frac{b}{d}\right)^{p_{\alpha,\beta}} \left(\frac{\sigma}{\mu_{\alpha,\beta}}\right)^{n_{\alpha,\beta}} \tag{11}$$

where the effective diffusion $D_{\alpha,\beta}$ can be expressed in the Arrhenius form

$$D_{\alpha,\beta} = D_0^{\alpha,\beta} \exp\left\{-\frac{Q_{\alpha,\beta}}{RT}\right\} \tag{12}$$

where $Q_{\alpha,\beta}$ is the apparent activation energy of each phase, $D_0^{\alpha,\beta}$ is the diffusion pre-exponential and p is the inverse grain size parameter. The shear modulus is expressed as a function of temperature according to [68] as

$$\mu_{\alpha,\beta} = \mu_{0_{\alpha,\beta}} \left(1 + \left(\frac{T - 300}{T_M}\right)\left(\frac{T_M}{\mu_{0_{\alpha,\beta}}} \frac{d\mu_{\alpha,\beta}}{dT}\right)\right) \tag{13}$$

where μ_0 is the shear modulus at 300 K and $T_M/\mu_0 d\mu/dT$ is its temperature dependent factor. The material parameters employed for both α and β phases are listed in Table 2.

The strain rate contributed by grain boundary sliding is generally expressed as [69].

$$\dot{\varepsilon}_{\text{gbs}} = \frac{A_{\text{gbs}} f_\beta^q D_{\text{gbs}} G b}{kT} \left(\frac{b}{d}\right)^{p_{\text{gbs}}} \left(\frac{\sigma}{\mu}\right)^{n_{\text{gbs}}}. \tag{14}$$

where n_{gbs} is the stress exponent due to superplastic grain boundary sliding, p_{gbs} is the inverse grain size parameter and q is a material parameter introduced to compensate the effect of the volume fraction of β-phase (q=0.44). Physical properties which depend on a uniformly dispersed aggregate of α and β phases are averaged following the rule of mixtures as

$$P_c = P_\alpha f_\alpha + P_\beta f_\beta \tag{15}$$

where P is the physical property and f is the volume fraction of each phase.

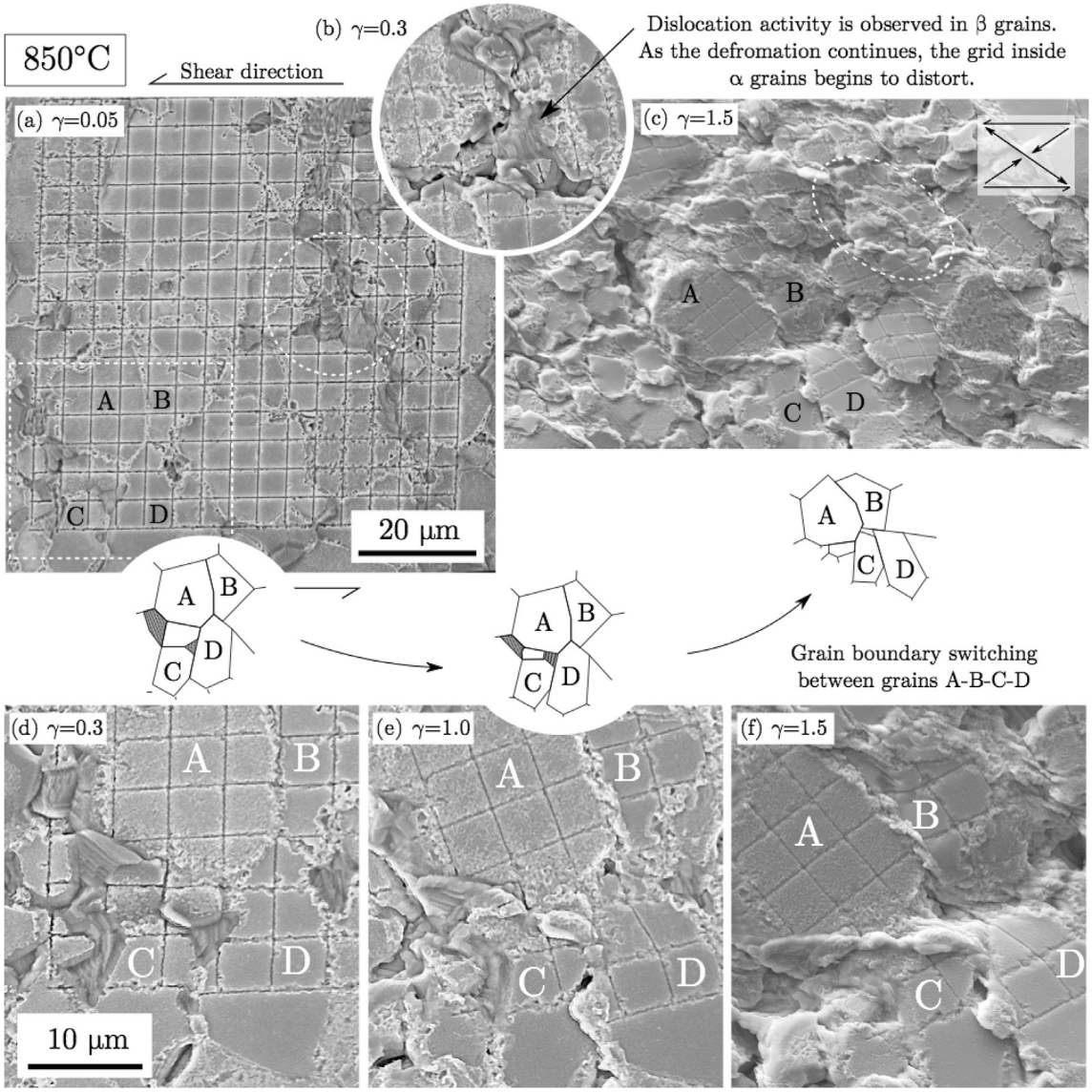

Fig. 11. Gridded region at different points during a shear test at 850 °C and a shear strain rate of 2×10^{-4}/s. Micrographs are presented at shear strain values of (a) γ=0.05 and (c) γ=1.5. A series of magnified illustrations detailing the grain neighbour switching process are presented at shear strains of: (d) γ=0.3, (e) γ=1.0 and (f) γ=1.5; (b) micrograph showing the lattice deformation of β phase for a shear strain of 0.3.

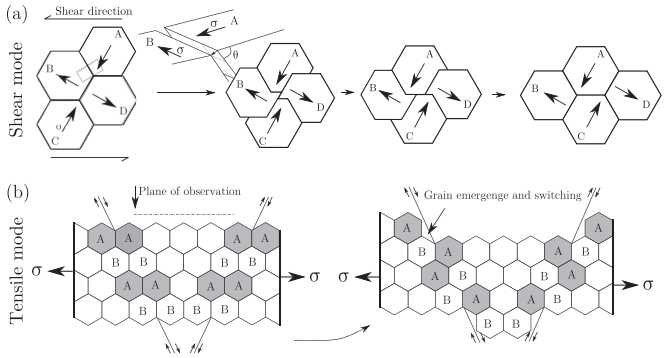

Fig. 12. Details of the grain neighbour switching process: (a) shear deformation switching with out-of-plane grain boundary sliding and (b) tensile deformation switching during emergence of interior grains [9].

The volume fraction of β phase can be expressed as [70]:

$$f_\beta = 1 - \exp\{-\theta^n\} \tag{16}$$

where f is the transformed β fraction, n is the Avrami constant and

$$\theta = \int_0^t k\{T\}dt \tag{17}$$

$$k(T) = k_0 \exp\left\{\frac{-Q}{RT}\right\} \tag{18}$$

where k_0 is a constant, Q is the activation energy, R is the gas constant and T is the temperature in Kelvin. The volume fraction of three different titanium alloys are represented using this equation, the parameters are listed in Table 3, its determination will be discussed in a further publication.

This set of equations has been calibrated to the experimentally obtained stress-strain rate data for three different alloys – Ti–6Al–4V, Ti54M and VST2K – following the same load-relaxation procedure. Two grain sizes were considered for each alloy, obtained through different heat-treatment conditions as

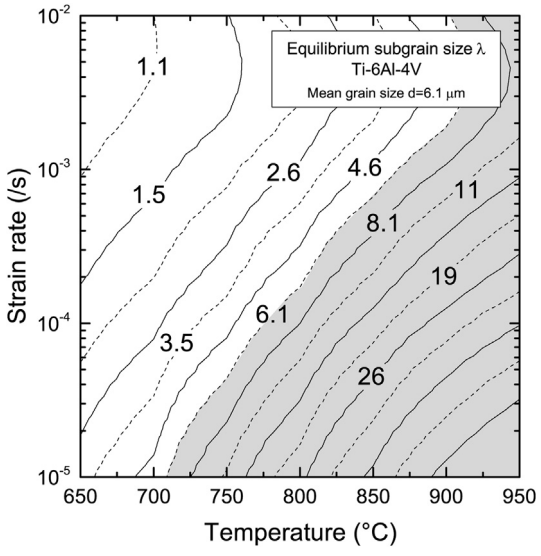

Fig. 13. Contour plot of the equilibrium subgrain size (λ) as function of temperature and strain rate for high temperature deformation of Ti–6Al–4V.

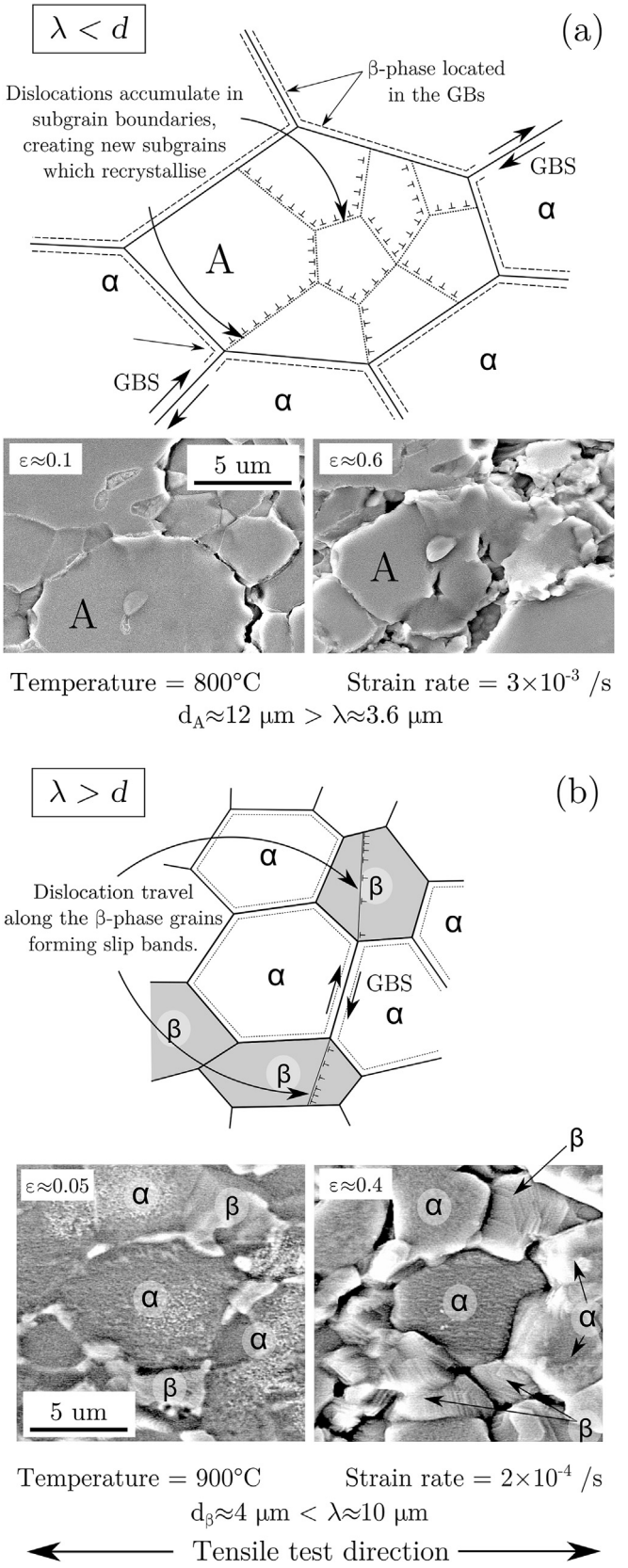

Fig. 14. Representative images showing the accommodation mechanism of Rachinger grain boundary sliding as a function of the subgrain size parameter λ: (a) equilibrium subgrain size less or equal than the mean grain size ($\lambda<d$) for a temperature of 800 °C and a strain rate of 3×10^{-3}/s. (b) equilibrium subgrain size greater than the mean grain size ($\lambda>d$) for a temperature of 900 °C and a strain rate of 5×10^{-4}/s.

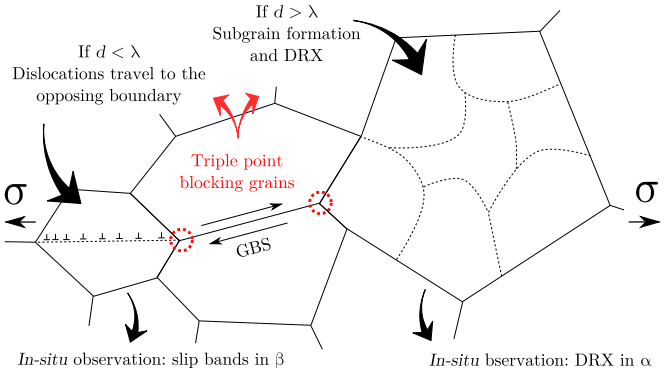

Fig. 15. Representation of the combination of possible accommodation mechanisms in Ti–6Al–4V as function of the grain size and equilibrium subgrain size parameter λ.

shown in Fig. 16. The parameter calibration was carried out using genetic-algorithm optimisation techniques [71]. The material parameters were fitted to the prior heat-treatment conditions – after heat-treatment experimental data were then used to assess the prediction capabilities of the model.

The results are shown in Fig. 17. It is found that the stress-strain rate response of the material is well explained by a combination of dislocation-creep accommodated grain boundary sliding and superplastic grain boundary sliding – the possible regimes for the Rachinger effect. In particular, the model is able to capture the change in the strain rate sensitivity parameter m as a function of strain-rate, temperature, grain size and β volume fraction by combining the strain contribution of each proposed mechanism. The optimised parameters are given in Table 4. The obtained stress exponents for intragranular creep in α and β phases are 5.21 and 4.07, consistently with climb-controlled dislocation creep. For grain boundary sliding, a stress exponent of 2.03 is found, close to the typical value for GBS-controlled superplasticity [1]. The activation energies for α and β intragranular mechanisms are 306 and 317 kJ/mol respectively. These estimates are higher than self-diffusion values for α and β phases, however, previous studies have shown that dynamic recrystallisation can increase the apparent activation energy in Ti–6Al–4V [46,52,72]. The activation energy for grain boundary sliding is 174 kJ/mol, in agreement with the values of grain boundary diffusion [68]. The results suggest that at high strain-rates (Region III), superplasticity is controlled by thermally-activated dislocation-climb processes followed by dynamic recrystallisation and at slower strain rates (Region II), superplastic grain boundary sliding dominates the deformation process.

6.2. Elucidation of the dominant deformation mechanism

A thermodynamic model based on the minimisation of energy dissipated by the system formed by each considered deformation mechanisms is proposed. The power balance of a system with constant temperature and balanced heat transfer (input heat = transmitted heat) can be expressed as

$$\dot{\psi} = W_e + \dot{\delta}_p \tag{19}$$

Table 2
Physical parameters for α and β titanium [68].

	b (m)	μ_0 (MN/m^2)	$T_m/\mu_0 d\mu/dT$	T_m (K)
α-phase	2.95×10^{-10}	4.36×10^{4}	−1.2	1933
β-phase	2.87×10^{-10}	2.05×10^{4}	−0.5	1933

Table 3
Material parameters used to represent the transformed fraction of β-phase as function of temperature for three titanium alloys assuming a heating rate of 1 °C/s.

	k_0	n	Q (J/mol)
Ti–6Al–4V	4.56×10^{4}	1.547	1.145×10^{5}
Ti54M	2.88×10^{4}	1.517	1.028×10^{5}
VST2K	2.99×10^{4}	1.384	1.018×10^{5}

where ψ is the free energy stored in the system per unit volume (elastic and internal energy) and W_e is the external mechanical power supplied to the system per unit volume – i.e. external forces through the boundary and internal body forces (negligible). The term $\dot{\delta}_p$ represents the energy dissipated by the system per unit of time and volume and is considered purely plastic. Here, the dissipation of energy is assumed to be a combination of each one of the present deformation mechanisms following

$$\dot{\delta}_p = \dot{\delta}_\alpha(\varepsilon_\alpha, f_\alpha) + \dot{\delta}_\beta(\varepsilon_\beta, f_\beta) + \dot{\delta}_{\text{gbs}}\left(\varepsilon_{\text{gbs}}\right) \tag{20}$$

where the dissipation terms are equal to the internal plastic work dissipated by each one of the three mechanisms causing plasticity. Thus

$$\delta = \int_{V_\alpha} \sigma\cdot\varepsilon_\alpha \, dV_\alpha + \int_{V_\beta} \sigma\cdot\varepsilon_\beta \, dV_\beta + \int_{V} \sigma\cdot\varepsilon_{\text{gbs}} \, dV. \tag{21}$$

Assuming homogeneous deformation of each phase and considering the energy per unit volume of material, the energy dissipated can be written as

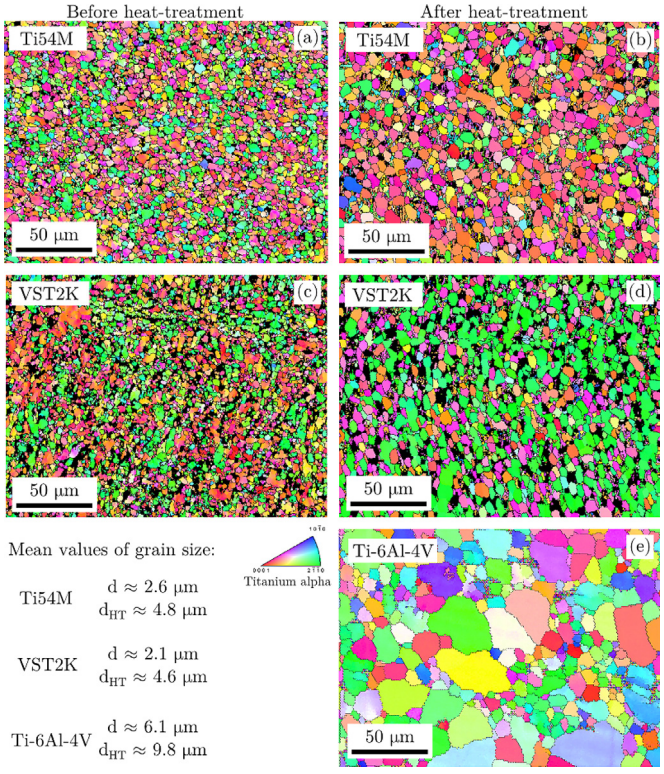

Fig. 16. Electron backscattered inverse pole figure maps for α titanium and mean grain size estimations for Ti54M, VST2K and Ti–6Al–4V titanium alloys before and after heat treatment.

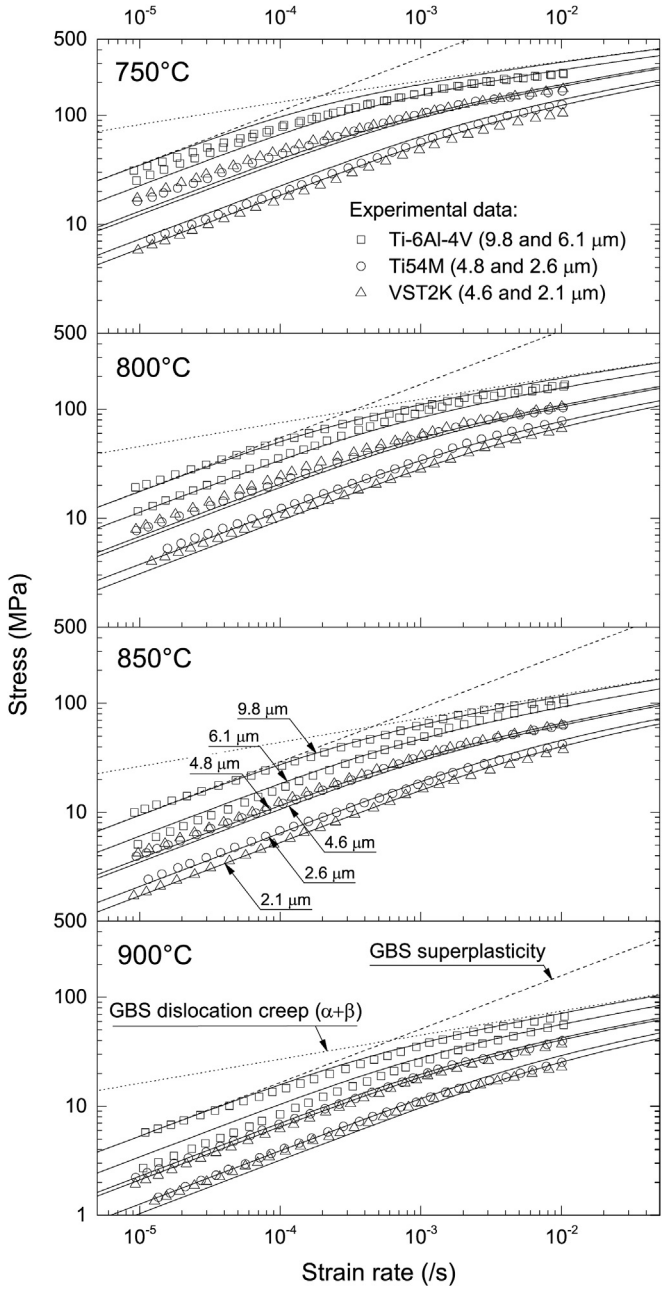

Fig. 17. Stress versus strain rate response of Ti–6Al–4V at: (a) 750 °C, (b) 800 °C, (c) 850 °C and (d) 900 °C. Graphs show the experimental data and results of the analytical model. The model results are decomposed for each one of the deformation mechanisms believed to be in operation.

$$\dot{\delta} = \sigma \cdot \varepsilon_\alpha \frac{V_\alpha}{V_t} + \sigma \cdot \varepsilon_\beta \frac{V_\beta}{V_t} + \sigma \cdot \varepsilon_{\text{gbs}} \tag{22}$$

where the stress σ of each operative mechanism can be extracted by solving Equations (11) and (14). The strain contribution of each mechanism is then non-dimensionalised to eliminate the dependence on the total strain ε_t so

$$\frac{\varepsilon_\alpha}{\varepsilon_t} + \frac{\varepsilon_\beta}{\varepsilon_t} + \frac{\varepsilon_{\text{gbs}}}{\varepsilon_t} = 1 \tag{23}$$

and the volume of each phase is assumed to vary as a function of the volume fraction of each phase as

$$\frac{V_\alpha}{V_t} = (1 - f_\beta) \tag{24}$$

$$\frac{V_\beta}{V_t} = f_\beta \tag{25}$$

Table 4
Optimised parameters for the proposed physically-based equations to represent the Rachinger boundary sliding effect. Diffusion pre-exponential values from Ref. [68].

	n	p	AD_0 [m^2 s^{-1}]	Q [kJ mol^{-1}]
GBS superplasticity	2.03	1.91	1.85×10^4	174
GBS with α dislocation creep	5.21	2.13	1.20×10^{18}	306
GBS with β dislocation creep	4.07	2.18	2.16×10^{18}	317

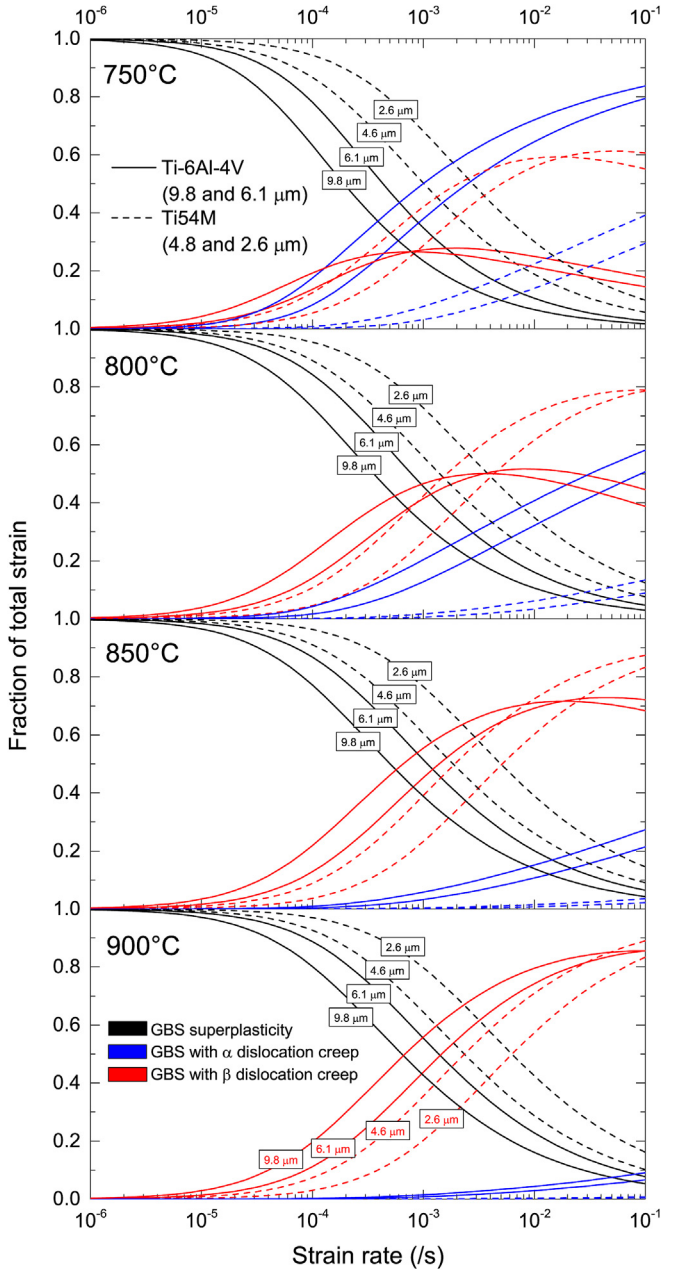

Fig. 18. Fraction of total strain contributed by each one of the operative deformation mechanisms as predicted by the equation of dissipated energy, for temperatures of: (a) 750 °C, (b) 800 °C, (c) 850 °C and (d) 900 °C.

$$\frac{V_{gbs}}{V_t} = 1. \quad (26)$$

The terms $\varepsilon_\alpha/\varepsilon_t$ and $\varepsilon_\beta/\varepsilon_t$ have been optimised using a gradient-based function so that the energy dissipated by the proposed system is minimised for each combination of strain rate and temperature. The results presented in Fig. 18 confirm the total strain contribution of each deformation mechanism. These are consistent with the rationalisation extracted from the surface observations in that: (i) there is a change from dislocation creep at high strain rates to superplastic grain boundary sliding at lower strain rates, (ii) an increase in temperature facilitates superplastic grain boundary sliding, (iii) a reduction of the mean grain size critically enhances superplastic grain boundary sliding and finally (iv) deformation of β facilitates the accommodation at every considered temperature, but only at high temperatures – when there is enough volume fraction of β – can the grain boundary sliding be accommodated without deformation of the α phase.

7. Conclusions

Novel, high-temperature *in-situ* SEM observations of superplasticity have provided conclusive insights into the mechanisms responsible for the superplastic effect in Ti–6Al–4V. The following specific conclusions can be drawn:

1. Rachinger grain boundary sliding (GBS) is shown to be the dominant accommodation process during the superplasticity of Ti–6Al–4V; thus the equilibrium subgrain size parameter λ is of profound importance.
2. When λ is greater than the mean grain size, d, Rachinger GBS occurs under superplastic conditions. If λ is smaller than d, dislocations pile-up in α forming subgrain boundaries eventually causing dynamic recrystallisation. This change in mechanism is supported by the *in-situ* surface observations, experimental measurement of the strain rate sensitivity parameter m and analytical modelling.
3. Changes in the volume fraction of the β phase are responsible for the transition from dislocation-creep to superplastic grain boundary sliding. At 850 and 900° C (m>0.45), the fraction of β is optimal. Dislocation activity is confined to the interior of β grains; α lattice dislocations and recrystallisation are not found and cavitation is minimal.
4. The rate of deformation plays a similar role; even at low temperatures (700° C) – provided the rate is slow enough – intragranular deformation can be reduced to levels consistent with superplasticity. However, in these cases – due to the lack of β phase – cavitation is observed.
5. For temperatures below 700° C, no superplasticity is found; deformation is characterised by classical plasticity: grains elongate proportionally to the macroscopic strain along the tensile direction and no grain boundary sliding is observed.
6. Similar findings have emerged from surface observations at 750 and 850° C made on shear specimens. In this case, the constrained conditions allow the direct observation of the grain neighbour switching process. Use of FIB-milled microgrids supports the conclusions: intragranular deformation in the α phase decreases as temperature increases but intragranular β deformation is always observed – regardless of the volume fraction of β phase.
7. A model which captures the observed phenomena – based on Rachinger boundary sliding and intragranular dislocation creep – is formulated. Equations are calibrated to data obtained using stress-relaxation tests. The set of equations captures accurately the dependence of strain rate sensitivity on both strain rate and temperature.
8. The contribution of each mechanism to the total fraction of macroscopic strain has been elucidated using a thermodynamically consistent approach, in which the total dissipated energy for each possible deformation mode is minimised.

Acknowledgements

The research was supported by the EPSRC under grant number EP/J013501/1, by the multifunctional high performance alloys for extreme environments program. The authors of this papers are grateful to the Advanced Forming Research Centre, University of Strathclyde, for providing the material. The authors acknowledge Innovate UK and Rolls-Royce plc which through the SAMULET2 programme funded this research. The authors appreciate the help and advice of Professor Alan Cocks of the University of Oxford.

References

[1] T.G. Langdon, Seventy-five years of superplasticity: historic developments and new opportunities, J. Mater. Sci. 44 (2009) 5998–6010.
[2] F.A. Mohamed, Micrograin superplasticity: Characteristics and utilization, Materials 4 (2011) 1194–1223.
[3] M. Ashby, R. Verrall, Diffusion-accommodated flow and superplasticity, Acta Metall. 21 (1973) 149–163.
[4] J. Spingarn, W. Nix, Diffusional creep and diffusionally accommodated grain rearrangement, Acta Metall. 26 (1978) 1389–1398.
[5] A. Geckinli, Grain boundary sliding model for superplastic deformation, Metal Sci. 17 (1983) 12–18.
[6] A. Arieli, A. Rosen, Superplastic deformation of Ti-6Al-4V alloy, Metall. Trans. A 8 (1977) 1591–1596.
[7] R. Valiev, T. Langdon, An investigation of the role of intragranular dislocation strain in the superplastic Pb-62% Sn eutectic alloy, Acta Metall. Mater. 41 (1993) 949–954.
[8] P. Bate, P. Blackwell, Surface marker behaviour in superplastic and non-superplastic tension of Al-4.5% Mg, Scr. Mater. 38 (1998) 901–907.
[9] M. Mayo, W. Nix, Direct observation of superplastic flow mechanisms in torsion, Acta Metall. 37 (1989) 1121–1134.
[10] A. Ghosh, R. Raj, Grain size distribution effects in superplasticity, Acta Metall. 29 (1981) 607–616.
[11] M. Zelin, A. Mukherjee, Cooperative phenomena at grain boundaries during superplastic flow, Acta Metallurgica Materialia 43 (1995) 2359–2372.
[12] M. Rust, R. Todd, Surface studies of Region II superplasticity of AA5083 in shear: Confirmation of diffusion creep, grain neighbour switching and absence of dislocation activity, Acta Mater. 59 (2011) 5159–5170.
[13] C. Boehlert, C. Cowen, S. Tamirisakandala, D. McEldowney, D. Miracle, In situ scanning electron microscopy observations of tensile deformation in a boron-modified Ti-6Al-4V alloy, Scr. Mater. 55 (2006) 465–468.
[14] A.D. Kammers, S. Daly, Self-assembled nanoparticle surface patterning for improved digital image correlation in a scanning electron microscope, Exp. Mech. 53 (2013) 1333–1341.
[15] J.L. Walley, R. Wheeler, M.D. Uchic, M.J. Mills, In-Situ mechanical testing for characterizing strain localization during deformation at elevated temperatures, Exp. Mech. 52 (2012) 405–416.
[16] W.A. Rachinger, Relative grain translations in the plastic flow of aluminium, J. Inst. Met. 81 (1952).
[17] I.M. Lifshitz, On the theory of diffusion-viscous flow of polycrystalline bodies, Sov. Phys. Jetp-Ussr 17 (1963) 909–920.
[18] A.K. Mukherjee, The rate controlling mechanism in superplasticity, Mater. Sci. Eng. 8 (1971) 83–89.
[19] A. Arieli, A. Mukherjee, A model for the rate-controlling mechanism in superplasticity, Mater. Sci. Eng. 45 (1980) 61–70.
[20] T. Alden, The origin of superplasticity in the Sn-5% Bi alloy, Acta Metall. 15 (1967) 469–480.
[21] W. Hotz, E. Ruedl, P. Schiller, Observation of processes of superplasticity with the scanning electron microscope, J. Mater. Sci. 10 (1975) 2003–2006.
[22] R.B. Vastava, T.G. Langdon, An investigation of intercrystalline and interphase boundary sliding in the superplastic Pb-62% Sn eutectic, Acta Metall. 27 (1979) 251–257.
[23] D. Attwood, P. Hazzledine, A fiducial grid for high-resolution metallography, Metallography 501 (1976) 483–501.
[24] D. Lee, On the nature of superplastic deformation in the Mg-Al eutectic, Acta Metall. 17 (1969) 1057–1069.
[25] A.E. Geckinli, C.R. Barrett, Superplastic deformation of the Pb-Sn eutectic, J. Mater. Sci. 11 (1976) 510–521.
[26] M. Rust, R. Todd, High resolution surface studies of superplastic deformation in shear and tension, Mater. Werkst. 39 (2008) 289–292.
[27] K. Sotoudeh, P. Bate, Diffusion creep and superplasticity in aluminium alloys,

Acta Mater. 58 (2010) 1909–1920.
[28] P.S. Bate, F.J. Humphreys, N. Ridley, B. Zhang, Microstructure and texture evolution in the tension of superplastic Al-6Cu-0.4Zr, Acta Mater. 53 (2005) 3059–3069.
[29] P.S. Bate, N. Ridley, B. Zhang, Mechanical behaviour and microstructural evolution in superplastic Al-Li-Mg-Cu-Zr AA8090, Acta Mater. 55 (2007) 4995–5006.
[30] H. Zhang, L. Zhang, X. Cheng, L. Xu, B. Bai, Superplastic behavior during warm deformation of martensite in medium carbon steel, Scr. Mater. 62 (2010) 798–801.
[31] H. Zhang, B. Bai, D. Raabe, Superplastic martensitic Mn-Si-Cr-C steel with 900% elongation, Acta Mater. 59 (2011) 5787–5802.
[32] H. Zhang, K.G. Pradeep, S. Mandal, D. Ponge, P. Choi, C.C. Tasan, D. Raabe, Enhanced superplasticity in an Al-alloyed multicomponent Mn-Si-Cr-C steel, Acta Mater. 63 (2014) 232–244.
[33] R. Panicker, A. Chokshi, R. Mishra, Microstructural evolution and grain boundary sliding in a superplastic magnesium AZ31 alloy, Acta Mater. 57 (2009) 3683–3693.
[34] J.A. Valle, M.T. Pérez-Prado, O.A. Ruano, Deformation mechanisms responsible for the high ductility in a Mg AZ31 alloy analyzed by electron backscattered diffraction, Metall. Mater. Trans. A 36 (2005) 1427–1438.
[35] J.C. Tan, M.J. Tan, Dynamic continuous recrystallization characteristics in two stage deformation of Mg-3Al-1Zn alloy sheet, Mater. Sci. Eng. A 339 (2003) 124–132.
[36] Y. Xun, F.A. Mohamed, Slip-accommodated superplastic flow in Zn-22 wt%Al, Philos. Mag. 83 (2003) 2247–2266.
[37] Y. Xun, F.A. Mohamed, Superplastic behavior of Zn-22%Al containing nano-scale dispersion particles, Acta Mater. 52 (2004) 4401–4412.
[38] J. Kim, J. Kim, Y. Lee, C. Park, C. Lee, Microstructural analysis on boundary sliding and its accommodation mode during superplastic deformation of Ti-6Al-4V alloy, Mater. Sci. Eng. A 263 (1999) 272–280.
[39] J.H. Kim, S. Semiatin, C.S. Lee, Constitutive analysis of the high-temperature deformation of Ti-6Al-4V with a transformed microstructure, Acta Mater. 51 (2003) 5613–5626.
[40] J. Kim, S. Semiatin, C. Lee, Constitutive analysis of the high-temperature deformation mechanisms of Ti-6Al-4V and Ti-6.85 Al-1.6 V alloys, Mater. Sci. Eng. A 394 (2005) 366–375.
[41] J. Kim, J. Kim, Y. Lee, C. Park, C. Lee, Microstructural analysis on boundary sliding and its accommodation mode during superplastic deformation of Ti-6Al-4V alloy, Mater. Sci. Eng. A 263 (1999) 272–280.
[42] C. Lee, S. Lee, J. Kim, Y. Chang, Mechanical and Microstructural Analysis on the Superplastic Deformation Behavior of Ti-6Al-4V Alloy, 2000.
[43] G. Rai, N.J. Grant, Observations of grain boundary sliding during superplastic deformation, Metall. Trans. A 14 (1983) 1451–1458.
[44] H. Naziri, R. Pearce, M. Brown, K. Hale, Microstructural-mechanism relationship in the zinc/aluminium eutectoid superplastic alloy, Acta Metall. 23 (1975) 489–496.
[45] R.B. Vastava, T.G. Langdon, An investigation of intercrystalline and interphase boundary sliding in the superplastic Pb-62% Sn eutectic, Acta Metall. 27 (1979) 251–257.
[46] M. Meier, A. Mukherjee, Consequences of using the average diffusivity in correlating the enhanced superplasticity of iron-modified Ti-6Al-4V, Scripta Metallurgica Materialia 25 (1991) 1471–1476.
[47] S.L. Semiatin, F. Montheillet, G. Shen, J.J. Jonas, Self-consistent modeling of the flow behavior of wrought alpha/beta titanium alloys under isothermal and nonisothermal hot-working conditions, Metall. Mater. Trans. A 33 (2002) 2719–2727.
[48] A. Barnes, Superplastic forming 40 years and still growing, J. Mater. Eng. Perform. 16 (2007) 440–454.
[49] S.L. Semiatin, P.N. Fagin, J.F. Betten, A.P. Zane, A.K. Ghosh, G.A. Sargent, Plastic flow and microstructure evolution during low-temperature superplasticity of ultrafine Ti-6Al-4V sheet material, Metall. Mater. Trans. A Phys. Metall. Mater. Sci. 41 (2010) 499–512.
[50] M. Nazzal, M. Khraisheh, Finite element modeling and optimization of superplastic forming using variable strain rate approach, J. Mater. Eng. 13 (2004) 691–699.
[51] G.A. Salishchev, E.A. Kudrjavtsev, S.V. Zherebtsov, S.L. Semiatin, Low temperature superplasticity of Ti-6Al-4V processed by warm multidirectional forging, in: 11th International Conference on Superplasticity in Advanced Materials, ICSAM 2012, July 3, 2012-July 5, 2012, vol. 735, 2013, pp. 253–258.
[52] M. Meier, D. Lesuer, A. Mukherjee, The effects of the α/β phase proportion on the superplasticity of Ti-6Al-4V and iron-modified Ti-6Al-4V, Mater. Sci. Eng. A 154 (1992) 165–173.
[53] K. Mingard, B. Roebuck, E. Bennett, M. Gee, H. Nordenstrom, G. Sweetman, P. Chan, Comparison of EBSD and conventional methods of grain size measurement of hardmetals, Int. J. Refract. Metals Hard Mater. 27 (2009) 213–223.
[54] R. Arrowood, A. Mukherjee, Stress Relaxation of a Eutectic Alloy in the Superplastic Condition, 1987.
[55] G. Murty, Stress relaxation in superplastic materials, J. Mater. Sci. 8 (1973) 611–614.
[56] S.L. Semiatin, P.N. Fagin, R.L. Goetz, D.U. Furrer, R.E. Dutton, Characterization of Plastic Flow Pertinent to the Evolution of Bulk Residual Stress in Powder-Metallurgy, Nickel-Base Superalloys, Metall. Mater. Trans. A 46 (2015) 3943–3959.
[57] R. Picu, A. Majorell, Mechanical behavior of Ti-6Al-4V at high and moderate temperatures - Part II : constitutive modeling, Mater. Sci. Eng. A 326 (2002) 306–316.
[58] G.G.E. Seward, S. Celotto, D.J. Prior, J. Wheeler, R.C. Pond, In situ SEM-EBSD observations of the hcp to bcc phase transformation in commercially pure titanium, Acta Mater. 52 (2004) 821–832.
[59] D. Bae, A. Ghosh, A planar simple shear test and flow behavior in a superplastic Al-Mg alloy, Metall. Mater. Trans. A 34 (2003) 2465–2471.
[60] G. Gurewitz, N. Ridley, A.K. Mukherjee, Elevated temperature cavitation in creep and superplasticity of Ti-6Al-4V alloy, in: Proceedings of ICF International Symposium on Fracture Mechanics, 1983, pp. 12–25.
[61] T.G. Langdon, Grain boundary sliding revisited: Developments in sliding over four decades, J. Mater. Sci. 41 (2006) 597–609.
[62] E. Alabort, D. Putman, R. Reed, Superplasticity in Ti-6Al-4V: Characterisation, modelling and applications, Acta Mater. 95 (2015) 428–442.
[63] J.E. Bird, A.K. Mukherjee, J.E. Dorn, D.G. Brandon, A. Rosen, Quantitative Relation between Properties and Microstructure, vol. 255, Israel Universities Press, Jerusalem, 1969, p. 1969.
[64] F. a. Mohamed, T.G. Langdon, Deformation mechanism maps for superplastic materials, Scr. Metall. 10 (1976) 759–762.
[65] A. Ball, M.M. Hutchison, Superplasticity in the aluminium-zinc eutectoid, Metal Sci. 3 (1969) 1–7.
[66] T.G. Langdon, Grain Boundary Sliding as a Deformation Mechanism During Creep, 1970.
[67] J.R. Leader, D.F. Neal, C. Hammond, The effect of alloying additions on the superplastic properties of Ti-6 pct Al-4 pct V, Metall. Trans. A 17 (1986) 93–106.
[68] H.J. Frost, M.F. Ashby, Deformation Mechanism Maps: the Plasticity and Creep of Metals and Ceramics, Pergamon press, 1982.
[69] T.G. Langdon, A unified approach to grain boundary sliding in creep and superplasticity, Acta Metall. Mater. 42 (1994) 2437–2443.
[70] S. Malinov, Z. Guo, W. Sha, a. Wilson, Differential scanning calorimetry study and computer modeling of β α phase transformation in a Ti-6Al-4V alloy, Metall. Mater. Trans. A 32 (2001) 879–887.
[71] M. Li, X. Shankun, Experimental investigation and numerical simulation of the grain size evolution during isothermal forging of a TC6 alloy, Mater. Sci. Technol. 21 (2005) 155–160.
[72] Y.G. Ko, C.S. Lee, D.H. Shin, S.L. Semiatin, Low-temperature superplasticity of ultra-fine-grained Ti-6Al-4V processed by equal-channel angular pressing, Metall. Mater. Trans. A 37 (2006) 381–391.